A method for recovering stratospheric minor species densities from the Odin/OSIRIS scattered-sunlight measurements

Ian C. McDade, Kimberly Strong, Craig S. Haley, Jacek Stegman, Donal P. Murtagh, and Edward J. Llewellyn

Abstract: A method for recovering minor species density profiles in the stratosphere from observations made with the OSIRIS (optical spectrograph and infrared imager system) instrument on the Odin satellite is described. The OSIRIS instrument measures limb radiances of scattered sunlight over the spectral range 2800 to 8000 Å, for tangent heights ranging from 10 to 100 km. We describe how the limb spectra may be processed using the DOAS (differential optical absorption spectroscopy) technique to derive apparent column densities for the minor atmospheric constituents O_3, NO_2, OClO, and BrO. We also show how these column densities, measured over a range of tangent heights, may be inverted using an iterative least-squares technique to determine the local density profiles. The procedures are illustrated using simulated limb radiances generated with a realistic OSIRIS instrument model.

PACS Nos.: 42.68Mj, 94.10Dy

Résumé : Nous présentons une méthode pour recouvrer les profils de densité de composés mineurs de la stratosphère à partir des observations faites avec le détecteur OSIRIS (spectrographe optique et systéme d'imagerie infrarouge) à bord du satellite Odin. OSIRIS a pour mission de mesurer la radiance du limbe terrestre due à la diffusion de la lumière solaire dans le domaine de 2800 à 8000 Å pour des altitudes allant de 10 à 100 km. Nous montrons comment les spectres du limbe peuvent être analysés par DOAS (spectroscopie optique d'absorption différentielle) pour en déduire les variations verticales de densité des constituents mineurs de l'atmosphère, O3, NO2, OClO et BrO. Nous montrons aussi comment ces distributions verticales, mesurées pour une gamme d'altitudes, peuvent être inversées par une technique de moindres carrés pour déterminer les profils locaux de densité.

Received 7 June 1999. Accepted 15 January 2000. Published on the NRC Research Press Web site at `http://cjp.nrc.ca/` on 4 April 2002.

I.C. McDade[1] and C.S. Haley. Centre for Research in Earth and Space Science, York University, 4700 Keele Street, Toronto, ON M3J 1P3, Canada.
K. Strong. Department of Physics, University of Toronto, 60 St. George Street, Toronto, ON M5S 1A7, Canada.
J. Stegman and D.P. Murtagh.[2] Department of Meteorology, University of Stockholm, S-106 91 Stockholm, Sweden.
E.J. Llewellyn. Department of Physics and Engineering Physics, University of Saskatchewan, 116 Science Place, Saskatoon, SK S7N 5E2, Canada.

[1]Corresponding author (email: mcdade@yorku.ca).
[2]Present Address: Department of Radio and Space Science, Chalmers University of Technology, SE-41296 Göteborg, Sweden.

 DOI: 10.1139/P01-152

Nous illustrons ici la procédure en utilisant des radiances de limbe générées par un modèle réaliste d'OSIRIS.

[Traduit par la Rédaction]

1. Introduction

OSIRIS (optical spectrograph and infrared imager system) is a Canadian instrument now flying on the Swedish–Canadian–French–Finnish Odin satellite [1, 2]. Odin is in a 97.8° inclination, Sun-synchronous near-terminator orbit, with ascending and descending nodes at 18:00 and 06:00 h, respectively. OSIRIS makes limb measurements of solar radiation scattered by the atmosphere during the daytime for the purposes of monitoring atmospheric composition and temperatures in the stratosphere and lower mesosphere. The OSIRIS measurements are made over the wavelength range of 2800 to 8000 Å, at a spectral resolution of about 10 Å, for tangent heights ranging from 10 to 100 km. One of the objectives of the OSIRIS instrument is to determine the local density profiles of the important minor atmospheric constituents O_3, NO_2, OClO, and BrO. In this paper, we describe one of the methods being developed to extract the O_3, NO_2, OClO, and BrO densities from the OSIRIS scattered-sunlight measurements. The method exploits (*i*) the DOAS (differential optical absorption spectroscopy) technique [3] to determine apparent column densities for each of the species as a function of tangent height, and (*ii*) an iterative least-squares (ILS) inversion algorithm to extract the O_3, NO_2, OClO, and BrO densities from the apparent column densities. An alternative method for extracting the O_3, NO_2, OClO, and BrO densities using the optimal estimation method of Rodgers [4] is described in a companion paper by Strong et al. [5].

2. DOAS processing of the Odin/OSIRIS observations

2.1. DOAS in a solar occultation case

To illustrate how the DOAS technique will be applied to the OSIRIS scattered-sunlight measurements, we first consider the related, but much more restrictive, observational technique of solar occultation. In solar occultation the intensity of the unattenuated solar radiation $I^o(\lambda)$ at wavelength λ is measured by a solar-pointing satellite instrument when the line of sight towards the Sun does not pass through the atmosphere. Subsequent measurements of the transmitted solar intensity, $I^{th}(\lambda)$, when the line of sight, defined by the tangent altitude th, passes through the atmosphere can be used to obtain the column density of any absorbing species along the line of sight. If only one species, with known absorption cross section $\sigma(\lambda)$ at wavelength λ, is responsible for the atmospheric attenuation of the sunlight, the column density along the line of sight, c^{th} (molecules/cm^2), can be readily obtained using the Beer–Lambert Law

$$\frac{I^{th}(\lambda)}{I^o(\lambda)} = \exp(-\sigma(\lambda)c^{th}) \quad \text{or} \quad c^{th} = \frac{\ln\left[\frac{I^o(\lambda)}{I^{th}(\lambda)}\right]}{\sigma(\lambda)} \tag{1}$$

where the dimensionless quantity $\sigma(\lambda)c^{th}$ is the optical depth, $D(\lambda)$. Note that in this discussion, we are ignoring instrumentation effects such as finite spectral resolution and are not including the effects of rotational Raman scattering.

Usually, more than one species absorbs at wavelength λ, and Rayleigh scattering by air molecules and scattering by atmospheric aerosols contribute to the extinction of the sunlight. This problem of having more than one absorbing species can be taken into account by making the observations over a range of wavelengths for which the individual absorption cross sections $\sigma_i(\lambda)$ vary. The effects of Rayleigh and aerosol extinction can be taken into account by recognizing that the Rayleigh and aerosol extinctions, represented by the Rayleigh and aerosol optical depths $e_R(\lambda)$ and $e_A(\lambda)$, are slowly varying functions of wavelength as opposed to the absorption cross sections $\sigma(\lambda)$, which are typically rich

in spectral structure. This is the basis of the DOAS approach [3], which assumes that the absorption cross-section spectrum, $\sigma(\lambda)$, can be represented by a component that varies slowly with wavelength, $\sigma^{s}(\lambda)$, and a differential component, $\sigma'(\lambda)$, which varies rapidly with wavelength, i.e.,

$$\sigma(\lambda) = \sigma^{s}(\lambda) + \sigma'(\lambda) \tag{2}$$

For a single absorbing species, the transmitted solar intensity $I^{th}(\lambda)$ can then be expressed as

$$I^{th}(\lambda) = I^{o}(\lambda) \exp\left\{-\left[\sigma^{s}(\lambda) + \sigma'(\lambda)\right] c^{th} - e_{R}^{th}(\lambda) - e_{A}^{th}(\lambda)\right\} \tag{3}$$

where $e_{R}^{th}(\lambda)$ and $e_{A}^{th}(\lambda)$ are the slowly varying Rayleigh and aerosol optical depths.

The total optical depth $D^{th}(\lambda)$, for a given tangent height, can then be written as

$$D(\lambda) = \ln\left[\frac{I^{o}(\lambda)}{I(\lambda)}\right] = \sigma'(\lambda)c + \left[\sigma^{s}(\lambda)c + e_{R}(\lambda) + e_{A}(\lambda)\right] \tag{4}$$

where the tangent height superscripts have been dropped for clarity.

If the measured total optical depth $D(\lambda)$ is resolved into its slowly and rapidly varying components $D^{s}(\lambda)$ and $D'(\lambda)$, the slowly varying component $D^{s}(\lambda)$ can be assigned to the slowly varying absorption and extinction components, i.e.,

$$D^{s}(\lambda) = \sigma^{s}(\lambda)c + e_{R}(\lambda) + e_{A}(\lambda) \tag{5}$$

and the rapidly varying, or differential, component $D'(\lambda)$ can be assigned to the rapidly varying component of the optical depth, i.e.,

$$D'(\lambda) = \sigma'(\lambda)c \tag{6}$$

The total column density of the absorbing species can then be obtained from

$$c = \frac{D'(\lambda)}{\sigma'(\lambda)} \tag{7}$$

where $D'(\lambda)$ is the rapidly varying component of the measured quantity $\ln[I^{o}(\lambda)/I(\lambda)]$.

For the case of more than one absorber, $D'(\lambda)$ can be expressed as

$$D'(\lambda) = \sigma_{1}'(\lambda)c_{1} + \sigma_{2}'(\lambda)c_{2} + \sigma_{3}'(\lambda)c_{3} + \cdots \tag{8}$$

and the actual column density of each species, c_1, c_2, etc., can be obtained by fitting the observed $D'(\lambda)$ spectrum to the differential spectra of the individual species using standard linear regression.

2.2. DOAS in the Odin/OSIRIS case

In the case of OSIRIS, we do not make a direct solar transmission measurement, as in an occultation experiment, but continuously measure the sunlight scattered by the atmosphere on the dayside of the orbit, thus greatly enhancing the global coverage of the observations. The OSIRIS limb measurements are made within the orbital plane, and for a true terminator orbit the scattering angle and the solar zenith angle at the tangent point would both be 90°. However, since the Odin inclination is 97.8° the orbit only coincides with the terminator twice per year (once in October and once in February) and the scattering angle and solar zenith angle vary between 58.7° and 121.3°. Owing to this observing geometry, we do not have a simple external source of radiation against which to register transmission, rather, we have a continuum of internal Rayleigh-scattering sources along the instrument line of sight. This can be thought of as a collection of discretized sources along the line of sight. The spectral distribution and radiance of each of these discretized internal sources, $I_{j}^{o}(\lambda)$, for a single-scattering atmosphere is determined by

Fig. 1. Daytime limb-radiance spectra calculated for tangent heights of 20, 40, 60, and 80 km at 1 Å spectral resolution using MODTRAN [6].

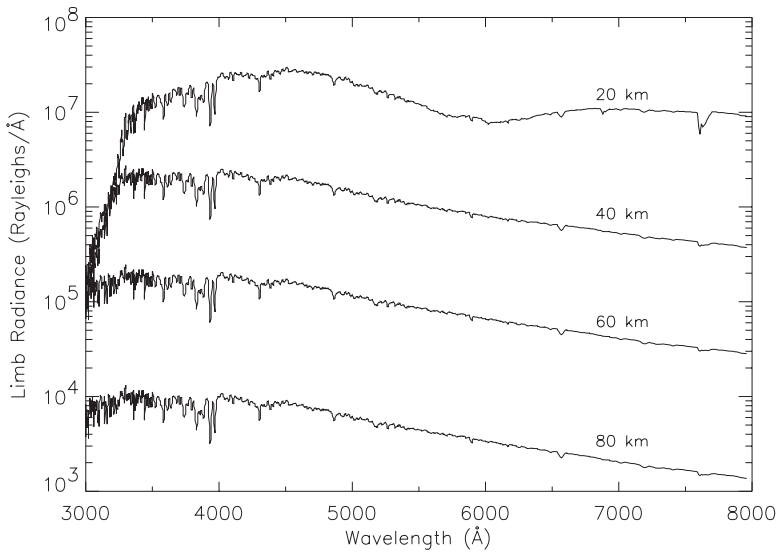

(*a*) the attenuation of the sunlight on its way in to each scattering point,

(*b*) the wavelength dependence of the Rayleigh-scattering cross section, and

(*c*) the density of the scattering molecules at point j.

For tangent heights above ~70 km the attenuation of the sunlight on its way in to each scattering point is negligible and the effective $I_j^o(\lambda)$ for each element along the line of sight for some lower tangent height can be characterized by a constant, B_j^{th}, times the spectral radiance $I^{\mathrm{ref}}(\lambda)$ measured at a reference tangent height of say 70 km, i.e.,

$$I_j^o(\lambda) = B_j^{th} I^{\mathrm{ref}}(\lambda) \tag{9}$$

where B_j^{th} depends on the tangent height and position of the jth source along the line of sight. By summing over all elements along a particular line of sight, we can define an effective $I^o(\lambda)$ for each tangent height as $I^o(\lambda) = B^{th} I^{\mathrm{ref}}(\lambda)$. Then by analogy with the standard DOAS approach described above in Sect. 2.1, it can be shown that for a single absorbing species

$$\ln\left[\frac{B^{th} I^{\mathrm{ref}}(\lambda)}{I^{th}(\lambda)}\right] = \sigma'(\lambda) c^{th} + \left[\sigma^{\mathrm{s}}(\lambda) c^{th} + e_{\mathrm{R}}^{th}(\lambda) + e_{\mathrm{A}}^{th}(\lambda)\right] \tag{10}$$

where $I^{th}(\lambda)$ represents the radiance observed at tangent height th and c^{th} is the apparent column density of the absorbing species along the line of sight. This apparent column density is determined in part by absorption on the way in from the Sun to each scattering point and by absorption on the way out from each scattering point towards OSIRIS.

By rearrangement of (10) we obtain

$$R^{th}(\lambda) = \sigma'(\lambda) c^{th} + \left[\sigma^{\mathrm{s}}(\lambda) c^{th} + e_{\mathrm{R}}^{th}(\lambda) + e_{\mathrm{A}}^{th}(\lambda) - \ln(B^{th})\right] \tag{11}$$

Fig. 2. Daytime limb-radiance spectra calculated with the MISU model for tangent heights of 20 and 70 km in the region where O_3, NO_2, OClO, and BrO are significant absorbers.

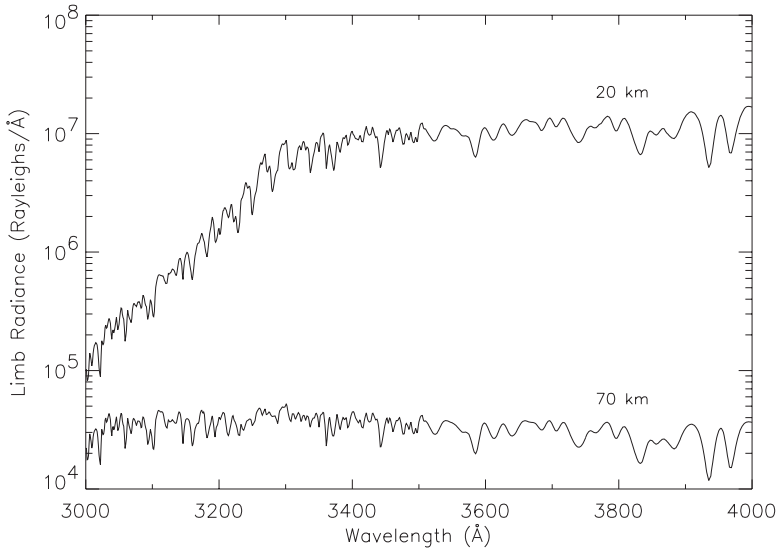

where $R^{th}(\lambda)$ is the natural logarithm of the ratio of $I^{\mathrm{ref}}(\lambda)$, the radiance observed at the reference altitude, and the radiance $I^{th}(\lambda)$ observed at the lower tangent altitude th, that is

$$R^{th}(\lambda) = \ln\left[\frac{I^{\mathrm{ref}}(\lambda)}{I^{th}(\lambda)}\right] \tag{12}$$

If $I^{\mathrm{ref}}(\lambda)$ and $I^{th}(\lambda)$ are measured over a finite wavelength range then $R^{th}(\lambda)$ can be resolved into its components that vary rapidly and slowly with wavelength and we obtain

$$R(\lambda) = R'(\lambda) + R^{\mathrm{s}}(\lambda) = \sigma'(\lambda)c + \left[\sigma^{\mathrm{s}}(\lambda)c + e_{\mathrm{R}}(\lambda) + e_{\mathrm{A}}(\lambda) - \ln(B)\right] \tag{13}$$

where the $e_{\mathrm{R}}(\lambda)$ and $e_{\mathrm{A}}(\lambda)$ terms represent the apparent Rayleigh and aerosol optical depths and the th superscripts have again been omitted for clarity.

By assigning the rapidly varying component of $R(\lambda)$ to the rapidly varying component of the absorber optical depth, i.e., $R'(\lambda) = \sigma'(\lambda)c$, we can obtain the absorber apparent column density from $c = R'(\lambda)/\sigma'(\lambda)$ at any wavelength.

For the case of more than one absorbing species we have

$$R'(\lambda) = \sigma'_1(\lambda)c_1 + \sigma'_2(\lambda)c_2 + \sigma'_3(\lambda)c_3 + \cdots \tag{14}$$

and the individual species apparent column densities, c_1, c_2, etc., for each tangent height can be obtained by least-squares fitting the differential ratio $R'(\lambda)$ spectrum to the individual differential cross-section spectra using linear regression.

2.3. Illustration of DOAS recovery for OSIRIS observations

To demonstrate how the DOAS approach can be applied to the OSIRIS observations we show in Fig. 1 modelled daytime limb-radiance spectra calculated using the MODTRAN code [6] at a spectral resolution of 1 Å for a number of tangent heights. Figure 1 shows how the radiances generally increase exponentially with decreasing tangent height and shows how absorption features appear at lower tangent

Fig. 3. The natural logarithm of the ratio of the 70 and 20 km tangent height radiance spectra shown in Fig. 2.

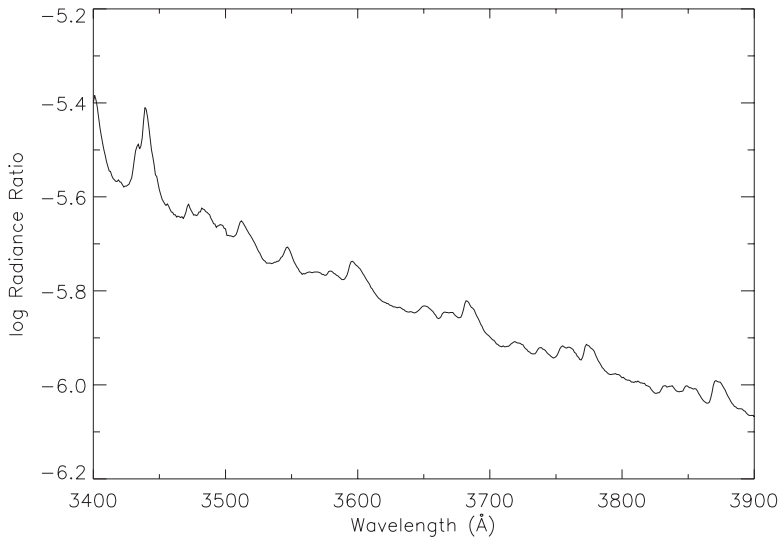

Table 1. DOAS fitting coefficients for a 20 km tangent height.

Absorber	Apparent column density
O_3	1.2×10^{20} molecules/cm^2
NO_2	1.3×10^{17} molecules/cm^2
OClO	4.2×10^{15} molecules/cm^2
BrO	4.0×10^{15} molecules/cm^2

heights. For example, in the 20 km spectrum, the broad O_3 Chappuis absorption between 5000 and 7000 Å and the narrower O_2 atmospheric (0-0) band absorption feature at 7620 Å are clearly evident.

Figure 2 shows more detailed 1 Å resolution 20 and 70 km tangent height spectra in the region where O_3, NO_2, OClO, and BrO are significant absorbers. The Fig. 2 spectra were obtained using the MISU (Meteorological Institute Stockholm University) single-scattering radiance model[3] which, unlike MODTRAN, incorporates absorption by O_3, NO_2, OClO, and BrO in the UV and visible regions. The radiances of Fig. 2 were calculated using a set of "standard" O_3, NO_2, OClO, and BrO density profiles for a nominal solar zenith angle of 80° and a scattering angle of 90°. For this study, aerosols were not included in the MISU model and a surface albedo of zero was adopted. Note that most of the obvious structure here arises from the structure in the solar spectrum and the decrease in the 20 km radiances below 3300 Å is due to strong absorption by O_3 and enhanced Rayleigh extinction.

In Fig. 3, we show the natural logarithm of the ratio of the 70 and 20 km radiances, i.e., $R(\lambda) = \ln[I^{\mathrm{ref}=70}(\lambda)/I^{th=20}(\lambda)]$, for the 3400 to 3900 Å region. The high-frequency structure here is due to the absorption signatures of O_3, NO_2, OClO, and BrO and the general increase in the ratio towards shorter wavelengths is due to the effects of Rayleigh extinction in the 20 km radiances.

One simple way to perform a DOAS analysis of the Fig. 3 radiance ratios, and to resolve $R(\lambda)$ into its slowly and rapidly varying components, is to pass a simple boxcar filter across $R(\lambda)$. The resulting

[3]J. Stegman and D.P. Murtagh. Private communication.

Fig. 4. The differential component of the Fig. 3 log ratio spectrum obtained as described in the text (continuous line). The symbols show the fit obtained using the O_3, NO_2, OClO, and BrO differential absorption cross sections and the fitting coefficients listed in Table 1.

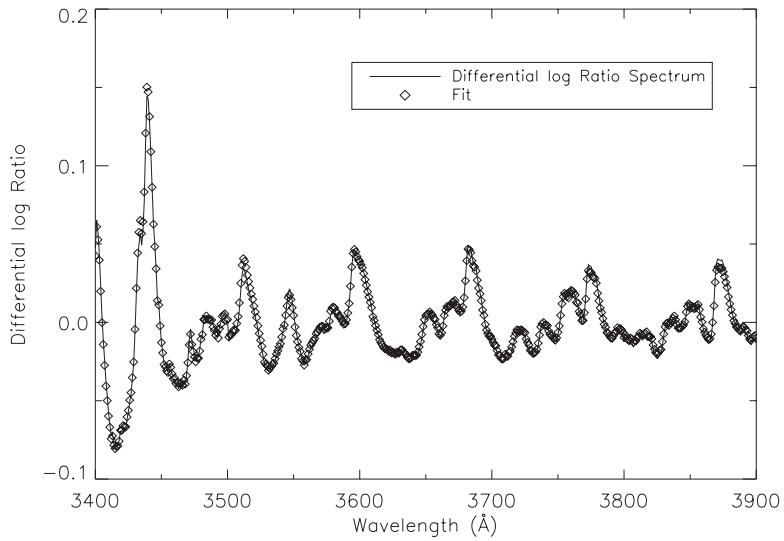

Fig. 5. The differential absorption spectra for O_3, NO_2, OClO, and BrO obtained as described in the text.

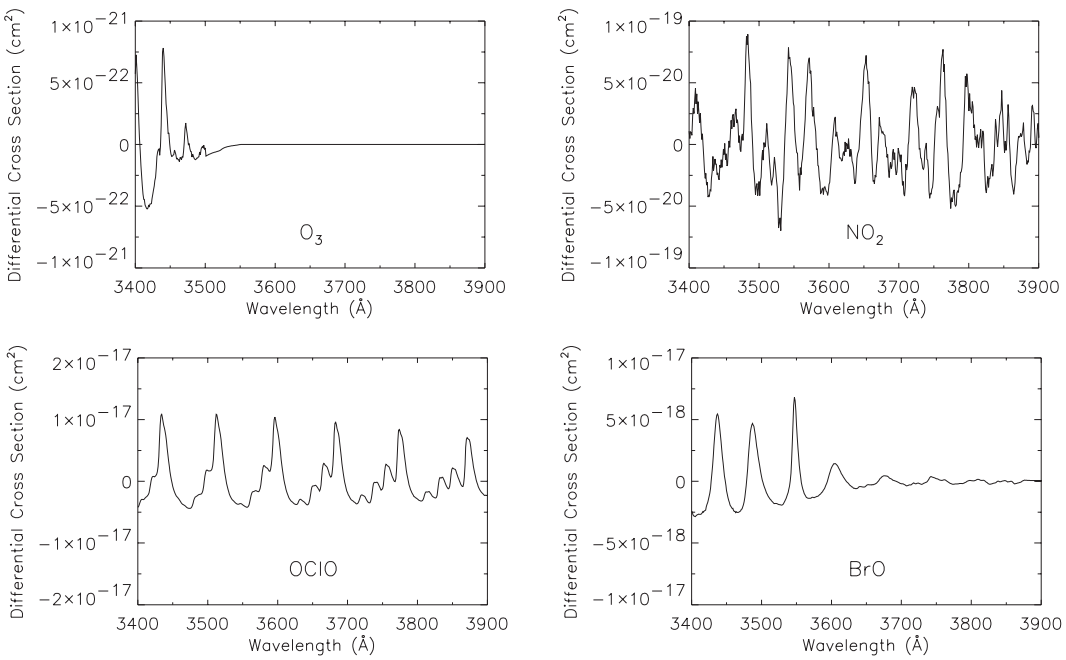

degraded spectrum is then subtracted from $R(\lambda)$ to obtain the differential component $R'(\lambda)$ required for the DOAS fit. The differential component thus obtained from the Fig. 3 values for $R(\lambda)$ using a 100 Å boxcar is shown in Fig. 4. The O_3, NO_2, OClO, and BrO differential absorption cross sections obtained in the same manner from the absolute cross sections of Molina and Molina [7], Schneider et al. [8], and Wahner et al. [9, 10], respectively, are shown in Fig. 5.

Fig. 6. The line-of-sight geometric weighting functions appropriate to a solar occultation experiment for tangent heights of 20, 40, and 60 km (left panel) and the OSIRIS scattered-sunlight weighting functions (right panel).

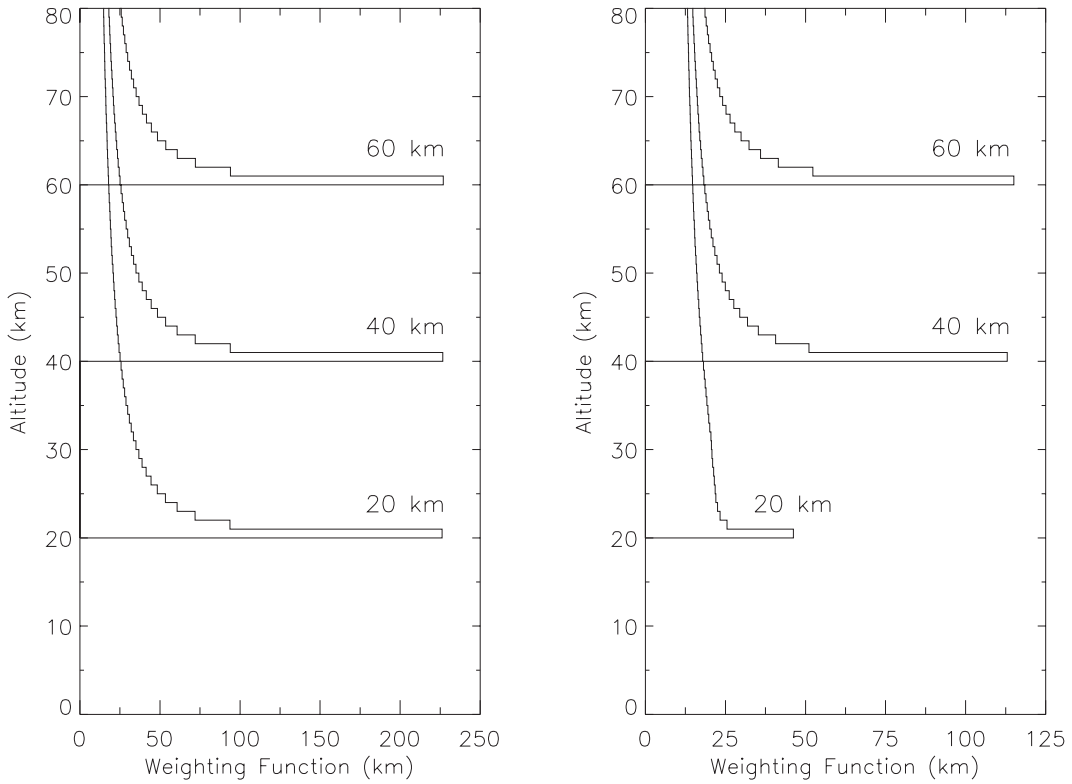

The final step in the DOAS process is to fit the differential log radiance ratios of Fig. 4 with the differential absorber cross sections of Fig. 5. The fitting coefficients from (14), obtained from a standard linear regression, provide the apparent column densities of O_3, NO_2, OClO, and BrO for the 20 km tangent height. The result of such a fit obtained with the O_3, NO_2, OClO, and BrO column densities listed in Table 1 is shown in Fig. 4.

By repeating this procedure using radiances measured at other tangent heights, profiles of the O_3, NO_2, OClO, and BrO apparent column densities can be obtained.

It should be noted that the apparent column densities thus obtained from scattered-sunlight limb radiances are not the same as the actual column densities along the instrument's geometric line of sight. The relationship between the apparent column densities and the line-of-sight column densities depends on the solar zenith angle and the spectral region used for the DOAS fit. For the case considered here, the actual column densities are about a factor of two larger than the apparent column densities.

3. Local density profiles from DOAS apparent column densities

To demonstrate how the O_3, NO_2, OClO, and BrO local number-density profiles can be extracted from a sequence of apparent column densities, obtained over a range of tangent heights, we again examine the problem in terms of the solar occultation analogue. For solar occultation, the relationship between the local density profiles and the measured sequence of column densities may be summarized as

$$\boldsymbol{C} = \boldsymbol{K}\boldsymbol{d} \tag{15}$$

where is $\boldsymbol{C}$ is an $m \times 1$ column vector representing the measured column densities of one specific species at m different tangent heights, $\boldsymbol{d}$ is an $n \times 1$ column vector representing the local densities of that species at n different altitudes, and $\boldsymbol{K}$ is an $m \times n$ weighting function matrix describing how the local densities at each altitude contribute to the column densities observed at each tangent height. For solar occultation, the K matrix is essentially made up of geometric path lengths through different atmospheric shells. For the case of $m = n$, the solution for the local number densities can formally be expressed as

$$\boldsymbol{d} = \boldsymbol{K^{-1}C} \tag{16}$$

where $\boldsymbol{K^{-1}}$ is the inverse of the K matrix in (15).

In the case of the OSIRIS measurements, a similar relationship exists between the DOAS apparent column densities and the absorber density profiles. However, the K-matrix elements, or weighting functions, cannot be determined simply from geometric considerations.

3.1. The K-matrix elements

One approach for obtaining the K matrices for the OSIRIS observations is to use a forward radiance model such as the MISU model. The forward model is used to determine the apparent DOAS column densities that would be observed at each tangent height for known O_3, NO_2, OClO, and BrO density profiles. The density profile for one species is then perturbed by a small amount at some altitude, h, and the apparent column density of that species is redetermined for all tangent heights. The resulting change in column density for each tangent height, th, is divided by the absolute density perturbation made at height h to provide one column of the K matrix for that species. By repeating this procedure for all heights the entire K matrix can be obtained for each species.

A limitation of this approach is that an accurate and reliable forward model is required and this model should take into account all of the relevant physics including multiple scattering and surface albedo effects. A second limitation is that the K-matrix elements are not entirely independent of the minor species densities. The magnitude of this nonlinearity depends on the spectral region used for the DOAS recovery. For the simulations discussed here, the nonlinearity effects are relatively weak.

Examples of DOAS weighting functions for ozone calculated using the MISU forward model for a number of tangent heights are shown in Fig. 6, where they are compared with the line-of-sight geometric weighting functions appropriate to an occultation experiment. Note that the scattered-sunlight weighting functions are smaller than the geometric line-of-sight functions. This is consistent with the DOAS column densities being smaller than the line-of-sight column densities as discussed in Sect. 2.3. Also note that the peak value of the DOAS weighting function for a tangent height of 20 km is smaller than that for the 40 and 60 km cases. This is due to larger Rayleigh extinction at lower tangent heights, which leads to shorter effective optical paths.

3.2. The matrix inversion

In the ideal case of perfect linearity, (15) also holds for OSIRIS observations. The solution density vector $\boldsymbol{d}$ can then be found by direct matrix inversion, (16). Direct inversions, however, are notoriously prone to noise in the observational data. An alternative approach that is particularly robust, noise tolerant, and computationally efficient is based on the iterative least-squares (ILS) method originally due to Budinger and Gullberg [11] and applied to atmospheric problems by McDade and Llewellyn [12]. This method is also used for the tomographic inversion of the IR imager observations made with the OSIRIS instrument [13]. An alternative approach based on the optimal estimation method of Rodgers [4] is discussed by Strong et al. [5].

The ILS algorithm starts with an initial guess $\boldsymbol{d'}$ for the actual solution density vector $\boldsymbol{d}$ and iteratively adjusts $\boldsymbol{d'}$ until the reconstructed observation vector $\boldsymbol{C'} = \boldsymbol{Kd'}$ agrees with the actual observation vector $\boldsymbol{C}$ to within the observational errors through a χ^2 minimization technique. The final solution is quite

Fig. 7. Simulated DOAS apparent column densities for O_3, NO_2, OClO, and BrO as a function of tangent height. Note that the MISU model used identical OClO and BrO density profiles for this simulation.

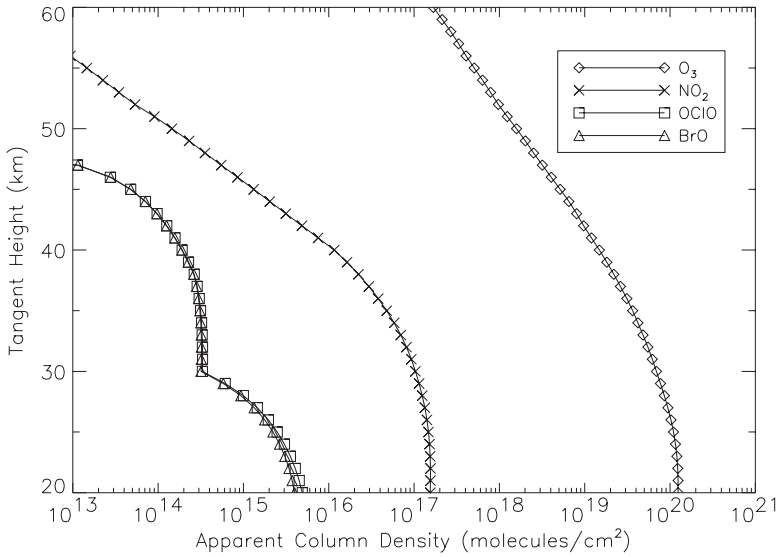

insensitive to the initial guess. Though the algorithm takes into account the estimated uncertainties in the observation vector, $\boldsymbol{\delta C}$, it should be noted that it does not provide useful statistics on the uncertainties in the solution vector.

To illustrate how the ILS inversion algorithm performs we consider the simulated O_3, NO_2, OClO, and BrO apparent column densities shown in Fig. 7. These column densities were obtained using the procedures described in Sect. 2 with radiances from the MISU forward model calculated at 1 Å resolution for a solar zenith angle of 80° and a scattering angle of 90°. The local number-density profiles recovered from the Fig. 7 apparent column densities using the ILS method are shown in Fig. 8 where they are compared with the actual O_3, NO_2, OClO, and BrO densities used in the MISU forward model. Note that for this simulation, OClO and BrO had identical density profiles within the MISU model. Clearly, for this high spectral resolution and noise-free simulation, the actual O_3, NO_2, OClO, and BrO densities are recovered with considerable fidelity, though small discrepancies, barely discernable in Fig. 8, do exist and arise from the weak nonlinearity.

4. OSIRIS simulations

The recoveries illustrated in the previous section do not take into account the effects of noise in the expected OSIRIS observations, nor do they include spectral degradation resulting from the actual instrument function. To assess how instrument noise and reduced spectral resolution will impact on the recoveries, a forward instrument model has been created to simulate the OSIRIS observations. Within this model, the MISU radiances are first convolved with a 10 Å boxcar to simulate the OSIRIS spectral resolution. The spectrally degraded radiances are then interpolated onto the nominal OSIRIS detector pixel wavelengths. The measured instrument flat-field responsivity (sensitivity to unpolarized light) is used to calculate the detected photon counts for each pixel assuming a specified integration time. Random Poisson noise is then added to each pixel count using the known detector characteristics – this allows for contributions from readout noise, photon shot noise, and dark current. As the OSIRIS instrument has 32 pixels for each wavelength bin, the individual pixel counts with noise added are summed in blocks of 32 to enhance the signal-to-noise ratio and to simulate the nominal OSIRIS operational mode. For each wavelength bin, uncertainties in the derived radiances are estimated using the procedures that will be

Fig. 8. The density profiles for O_3, NO_2, OClO, and BrO recovered from the ILS inversion of the Fig. 7 apparent column densities (symbols) and the actual densities used in the MISU forward model (continuous lines). Note that the actual OClO and BrO densities used for the simulation were the same.

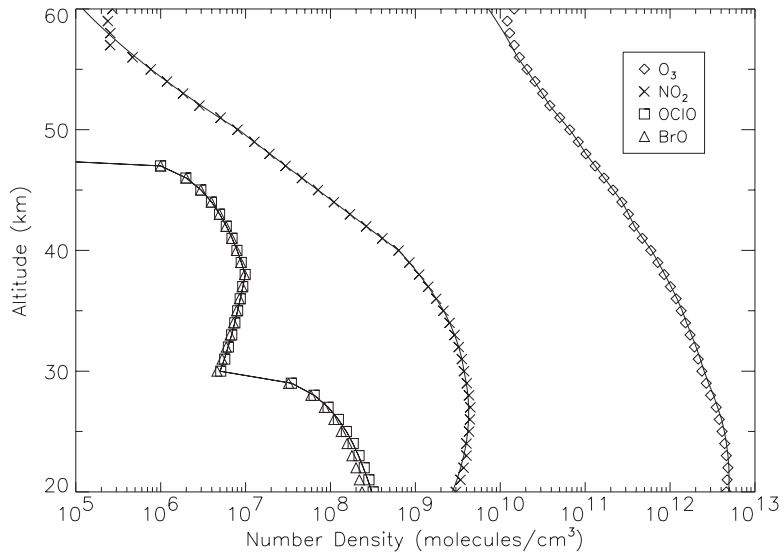

Fig. 9. A 30 km tangent height differential log ratio spectrum for the simulated OSIRIS radiances with noise and spectral resolution effects included (continuous line). The fit to the differential O_3, NO_2, OClO, and BrO absorption cross sections is shown by the symbols.

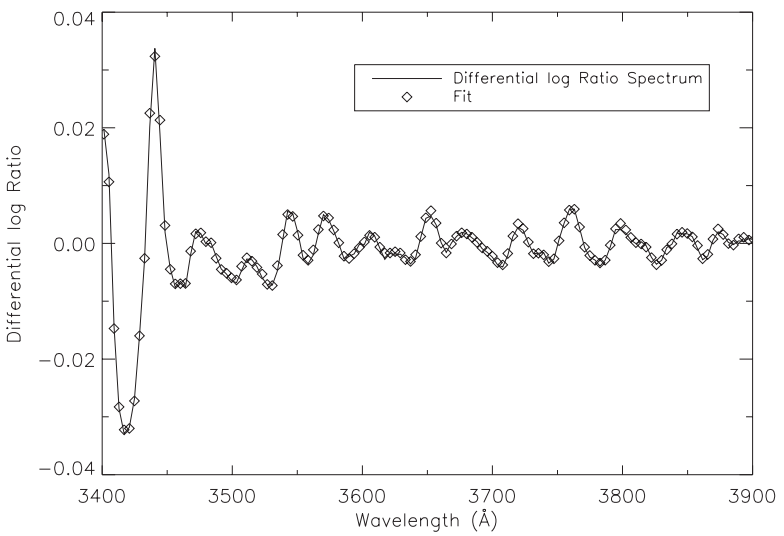

used for the processing of the actual OSIRIS data. Recoveries performed using the simulated OSIRIS radiances allow us to assess the precision with which O_3, NO_2, OClO, and BrO number densities may be obtained. For the DOAS processing of the simulated radiances, the absolute O_3, NO_2, OClO, and BrO absorption cross sections are also degraded to the instrument resolution and interpolated to the OSIRIS pixel wavelengths.

Figure 9 shows a typical simulated differential log ratio spectrum for a tangent height of 30 km together with the results of the DOAS fit to the O_3, NO_2, OClO, and BrO differential cross sections.

Fig. 10. The O_3, NO_2, OClO, and BrO apparent column density profiles obtained from the OSIRIS simulations that take into account the spectral resolution and noise characteristics of the instrument (symbols). The continuous lines show the column densities obtained without the effects of noise included.

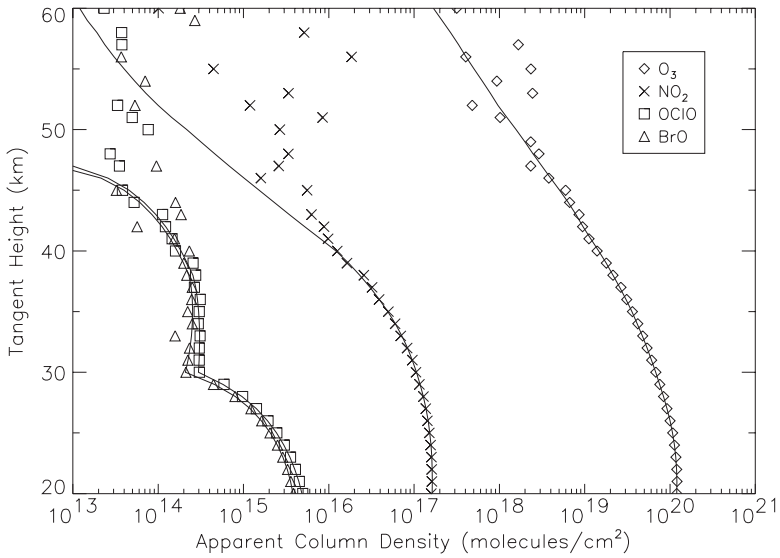

For this simulation, a noise-free 70 km spectrum was adopted as the reference. No noise was added to this 70 km spectrum since the reference spectra used for processing the actual OSIRIS data will be accumulated from a large number of high-altitude measurements. Note that the effects of noise are barely apparent in Fig. 9 but they do become apparent in the spectra for higher tangent heights. It should also be noted that Fig. 9 differs from Fig. 4 because of the lower spectral resolution of the former and different absorber signatures at 20 and 30 km. Figure 10 shows the O_3, NO_2, OClO, and BrO apparent column density profiles recovered from one complete simulated OSIRIS limb scan with DOAS processing of the limb radiances in the 3400 to 3900 Å region. These limb radiances were obtained for an integration time of 1 s at each tangent height and an Odin limb scan rate of 1 km/s.

Figure 11 shows the ozone number-density profile recovered from the ILS inversion of the ozone column densities shown in Fig. 10. Figure 11 also shows the actual ozone densities used in the MISU forward model. As noted above, the ILS algorithm does not provide error estimates for the recovered number densities. However, these errors may be estimated from the standard deviation of the densities recovered from a number of independent simulations performed using different sequences of random noise. The error bars on Fig. 11 indicate the estimated 1-σ uncertainties based on the standard deviation of the densities recovered at each height from 25 independent runs. Figure 11 shows that the ozone densities should be recoverable from a single OSIRIS limb scan with a precision of approximately $\pm 1\%$ between 20 and 30 km and better than $\pm 10\%$ between 30 and 40 km. This is more clearly illustrated in Fig. 12, which shows the 1-σ uncertainties expressed as a percentage of the actual ozone densities. At high altitudes the recovery is degraded due to reduced signal to noise in the measured radiance spectra and decreasing absorber signatures. It should be noted, however, that the precision at higher altitudes can be significantly improved with a separate DOAS analysis of radiances measured at shorter wavelengths where the ozone absorption signature is stronger. At lower altitudes, the uncertainties increase slightly because of increasing Rayleigh extinction, which reduces the magnitude of the weighting functions.

Figure 12 also shows the estimated percentage uncertainties associated with the NO_2 and OClO density recoveries. The BrO uncertainties are very similar to those for OClO and have, therefore, been omitted from Fig. 12 for clarity. In the case of NO_2, the recovery precision is not as good as for ozone. This is because even though the NO_2 differential cross sections are about a factor of 100 stronger, the

Fig. 11. The O_3 number densities recovered from the ozone apparent column densities of Fig. 10 that included noise (symbols) and the actual densities used in the MISU forward model (continuous line). The error bars show the 1-σ uncertainties based on the RMS deviation of the densities recovered at each altitude from 25 independent runs as described in the text.

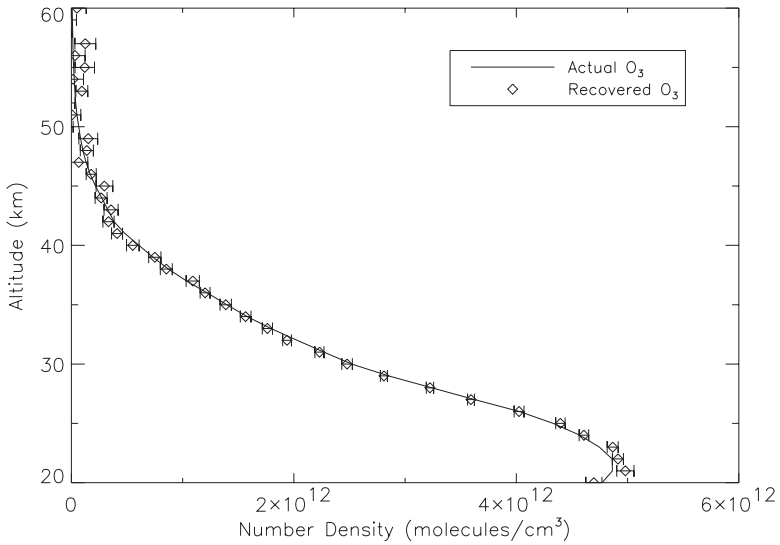

Fig. 12. The RMS deviation of the O_3, NO_2, and OClO densities recovered from 25 independent runs expressed as a percentage of the true densities at each height.

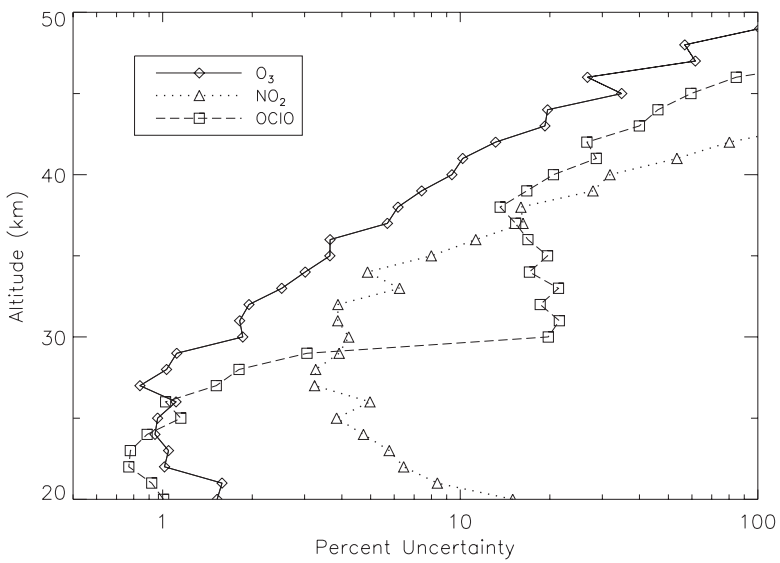

NO_2 densities used in the simulation are about a factor of 1000 smaller than ozone. As a result the NO_2 DOAS signature is about a factor of 10 smaller. For OClO and BrO the recovery precision is comparable to that for ozone in the 20 to 30 km region where their DOAS absorption signatures are similar to the ozone DOAS signature. At about 30 km the OClO and BrO uncertainties show a sharp increase which results from the sudden decrease in the OClO and BrO densities used in the MISU model (see Fig. 8). It should be noted that stratospheric OClO and BrO densities are highly variable and the ultimate precision with which the OClO and BrO densities will be recovered from the OSIRIS measurements will depend

on the actual densities encountered during the Odin mission.

5. Conclusions

A method for recovering O_3, NO_2, OClO, and BrO densities from OSIRIS scattered-sunlight measurements has been described. The method has been illustrated for the scenario of single scattering, no aerosols, and zero surface albedo. Procedures are presently being developed for dealing with multiple scattering, aerosols, and surface albedo effects using more sophisticated forward radiance models such as that described by McLinden et al. [14]. Preliminary results indicate that surface albedo and multiple-scattering effects introduce enhanced absorber signatures in the high-altitude reference spectrum. However, this effect is also reflected in the K-matrix elements obtained by perturbing a multiple-scattering forward radiance model and we find that the actual absorber density profiles can still be recovered when multiple-scattering effects are taken into account. Procedures are also being developed for dealing with nonlinearity, rotational Raman scattering (see ref. 15), and polarization effects.

Acknowledgements

Support for this work from the Canadian Space Agency and the Natural Sciences and Engineering Research Council of Canada is gratefully acknowledged.

References

1. E.J. Llewellyn, D.A. Degenstein, I.C. McDade et al. *In* Applications of photonic technology. *Edited by* G.A. Lampropoulos and R.A. Lessard. Plenum Press, New York. 1997. pp. 627–632.
2. D.P. Murtagh, U. Fisk, F. Merino et al. Can. J. Phys. **80** (2002). This issue.
3. U. Platt. *In* Air monitoring by spectroscopic techniques. *Edited by* M.W. Sigrist. John Wiley, New York. 1994. pp. 27–84.
4. C.D. Rodgers. Rev. Geophys. Space Phys. **14**, 609 (1976).
5. K. Strong, B.M. Joseph, R. Dosanjh, I.C. McDade, C.A. McLinden, J.C. McConnell, J. Stegman, D.P. Murtagh, and E.J. Llewellyn. Can. J. Phys. **80** (2002). This issue.
6. A. Berk, L. Bernstein, and D. Robertson. MODTRAN: A moderate resolution model for LOWTRAN 7. AFGL Tech. Rep. F19628-86-C-0079. Air Force Geophysics Laboratory, Hanscom AFB, Mass. 1989.
7. L.T. Molina and M.J. Molina. J. Geophys. Res. **91**, 14 501 (1986).
8. W. Schneider, G.K. Moortgat, G.S. Tyndall, and J.P. Burrows. J. Photochem. Photobiol. A: Chemistry **40**, 195 (1987).
9. A. Wahner, G.S. Tyndall, and A.R. Ravishankara. J. Phys. Chem. **91**, 2734 (1987).
10. A. Wahner, A.R. Ravishankara, S.P. Sander, and R.R. Friedl. Chem. Phys. Lett. **152**, 507 (1988).
11. T.F. Budinger and G.T. Gullberg. IEEE Trans. Nucl. Sci. **NS-21**, 2 (1974).
12. I.C. McDade and E.J. Llewellyn. Can. J. Phys. **69**, 1059 (1991).
13. D. Degenstein. Ph.D. thesis, University of Saskatchewan, Saskatoon, Sask. 1999.
14. C.A. McLinden, J.C. McConnell, E. Griffioen, and C.T. McElroy. Can. J. Phys. **80** (2002). This issue.
15. C.E. Sioris, W.F.J. Evans, R.L. Gattinger, I.C. McDade, D. Degenstein, and E.J. Llewellyn. Can. J. Phys. **80** (2002). This issue.